Challenges of Predicting Low-Latitude Ionospheric Scintillations

Archana Bhattacharyya

Centre of Studies in Resource Engineering
Indian Institute of Technology
Bombay, Powai, Mumbai, India
E-mail: archana.bhattacharyya@gmail.com

Abstract

Two regions of the globe that are most affected by ionospheric scintillations are the auroral region and the low-latitude region encompassing the dip equator. Our present-day dependence on satellite-based communication and navigation has led to a resurgence of interest in the prediction of ionospheric scintillations, which degrade the performance of such systems. In the low-latitude ionosphere, the genesis of intermediate-scale (~100 m to a few km) irregularities, which cause the most severe scintillations on VHF to L-band trans-ionospheric radio signals, is in the growth of the Rayleigh-Taylor (R-T) plasma instability on the bottom-side of the post-sunset equatorial F layer. Theoretical developments and observations by various ground-based instruments, as well as in-situ measurements by instruments onboard rockets and satellites, have identified several parameters of the ambient ionosphere that play key roles in the occurrence of these irregularities over the dip equator. However, the presence of basic conditions for the linear growth of the Rayleigh-Taylor instability fails to explain the large day-to-day variability in the characteristics of these irregularities, which determines the latitudinal distribution and strength of scintillations, and is a result of the nonlinear evolution of the Rayleigh-Taylor instability. In this paper, the present status of the efforts at prediction of low-latitude scintillations on the basis of a multitude of observations and numerical simulation of the development of the Rayleigh-Taylor instability in the equatorial ionosphere are reviewed. In particular, this review describes how observations of ionospheric scintillations may be used to obtain information about the nonlinear evolution of the Rayleigh-Taylor instability under different ambient conditions, which is yet to be explored through numerical simulation of the phenomenon. Such studies have pointed out important gaps in our knowledge about the evolution of equatorial ionospheric irregularities that are responsible for producing scintillations on L-band signals recorded in the equatorial and low-latitude regions around the globe.

1. Introduction

The initiation process for the development of irregularities in the post-sunset equatorial and low-latitude ionospheric plasma that give rise to fluctuations or scintillations in the amplitude and phase of trans-ionospheric VHF and higher frequency radio signals is well known. The presence of irregularities in the equatorial F-region ionosphere that affected the propagation of such radio waves in this region was first seen in ionosonde observations, where the reflected signals showed a "spread" in frequency or range [1]. All the irregularities that occurred in the equatorial F region thus came to be termed equatorial spread F (ESF) irregularities. Dungey [2] was the first to propose that the Rayleigh-Taylor (R-T) instability was responsible for the initiation of equatorial spread F irregularities on the bottom-side of the post-sunset equatorial F region. However, the first observations of the equatorial spread F phenomena from the Jicamarca Radio Observatory (JRO) in Peru brought out the inadequacies of the theories existing at the time for explaining the observations, particularly radar observations indicating the presence of irregularities on the topside of the post-sunset equatorial ionosphere [3]. A breakthrough came with the numerical simulation of the nonlinear development of the collisional Rayleigh-Taylor instability, when a plasma-depleted bubble rises to the linearly stable topside of the equatorial ionosphere [4]. Plumes seen in the range-time-intensity (RTI) maps obtained at Jicamarca Radio Observatory, as well as simultaneous in-situ measurements by a rocket-borne probe, optical observations of a barium cloud released from the rocket, and radar measurements made in Brazil, during equatorial spread F conditions were explained on the basis of upward-moving equatorial plasma bubbles (EPBs) rising from the bottom-side of the post-sunset equatorial F region [5, 6]. Simultaneous measurements of the vertical profile of plasma density using the PLUMEX I rocket probe and the range-time-intensity map of the back-scattered signal of the ALTAIR radar at Kwajalein
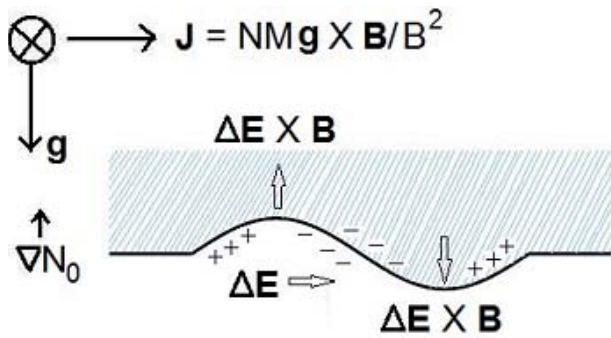
Figure 1. A schematic representation of the initiation of the Rayleigh-Taylor instability on the bottom-side of the post-sunset equatorial F region.

showed that the source region of the strongly back-scattered signal was co-located with a density-depleted region [7]. Similar results emerged from a comparison of ALTAIR range-time-intensity maps with horizontal plasma-density profiles obtained from the Atmospheric Explorer E (AE-E) satellite in-situ data [8]. The picture that emerged was thus that as the equatorial plasma bubbles rise to the top-side of the equatorial F-region in the nonlinear phase of growth of the Rayleigh-Taylor instability, the equatorial ionosphere becomes highly structured, with structures ranging in scale size from hundreds of kilometers down to a few centimeters. As the Rayleigh-Taylor instability involves interchange of entire magnetic flux tubes, an equatorial plasma bubble is elongated along the geomagnetic field. The geomagnetic-field-aligned nature of equatorial plasma bubbles was also established by observations from ALTAIR, a fully steerable radar [9].

The irregularities or structures appearing at different heights in the F region above the dip equator map along the geomagnetic field lines to off-equatorial latitudes. Out of the extended range of spatial scales associated with structures within equatorial plasma bubbles, irregularities with scale sizes in the intermediate range (~100 m to a few km) scatter VHF and higher-frequency radio waves that propagate through the equatorial and low-latitude ionosphere. This scattering produces a spatial pattern of signal amplitude and phase variations in the plane of the receiver. Movement of the irregularities relative to the signal path – either due to drift of the irregularities across the path of a signal transmitted from a geostationary satellite, or due to the signal path sweeping across irregularities as in the case of signals transmitted from orbiting satellites – causes the spatial patterns of signal amplitude and phase variations to move past the receiver. This results in temporal fluctuations in amplitude and phase of the signal recorded by a receiver, which are referred to as scintillations [10, 11]. Strong scintillations, causing deep fades of signal intensity, can result in loss of signal, and rapid phase fluctuations can cause loss of lock for the signal. Intermediate-scale-size irregularities associated with the equatorial plasma bubbles may cover a large part of the low-latitude ionosphere in

a particular longitude region on a given night. Therein lies their considerable potential for causing degradation in the performance of satellite-based communication and navigation systems [12]. With the advent of the Global Positioning System (GPS) and later Global Navigation Satellite Systems (GNSS), and large-scale technological dependence on these for navigation, there was a resurgence of interest in the study of ionospheric irregularities and the prediction of scintillations, particularly on L-band signals. Studies of the global distribution of scintillation activity have identified two regions of the globe to be most vulnerable to ionospheric scintillations: the auroral region, and the low-latitude region extending from the dip equator to the equatorial-ionization-anomaly (EIA) regions in both the hemispheres [13, 14]. The physical processes that give rise to scintillation-producing ionospheric irregularities in these two regions are different. As noted earlier, the Rayleigh-Taylor instability initiated on the bottom-side of the post-sunset equatorial F region has been identified as the basic plasma process that ultimately leads to the development of scintillation-producing irregularities in the equatorial and low-latitude ionosphere. The Rayleigh-Taylor instability and scintillations produced by ionospheric irregularities associated with this instability have been studied for several decades. However, the day-to-day variability in the occurrence of these irregularities, their latitudinal extent, and their spatial characteristics, which play critical roles in causing scintillations on signals in different frequency bands, create challenges for prediction of scintillations in the low-latitude regions. Some specific challenges and recent progress made towards identifying the conditions that contribute to the day-to-day variability of not only the occurrence pattern of scintillations but also the latitudinal distribution of scintillations on radio signals of different frequencies are discussed in the next few sections of this article.

2. Seeding of the Rayleigh-Taylor Instability

The process of initiation of the Rayleigh-Taylor instability on the bottom side of the post-sunset equatorial F-region – where the geomagnetic field, $\mathbf{B}$, is horizontal and northward, and a steep upward gradient, ∇N_0, exists in the ambient plasma density, N_0 – is shown in Figure 1. Under the influence of gravity and the geomagnetic field, ions move eastward. Westward movement of the much lighter electrons is negligible, and there is a net eastward current, $\mathbf{J} = N M \mathbf{g} \times \mathbf{B} / \mathrm{B}^2$, where N is the local plasma density. A perturbation on the bottom-side causes this current to have a divergence, and as a result, charges pile up as shown, producing an eastward-directed perturbation electric field, $\Delta \mathbf{E}$, in the region where plasma density is lower. This electric field gives rise to an upward $\Delta \mathbf{E} \times \mathbf{B}$ drift of the plasma-depleted region, creating an upward-moving equatorial plasma bubble. The linear growth rate of the Rayleigh-Taylor instability showed the importance of the pre-reversal enhancement (PRE) of the eastward
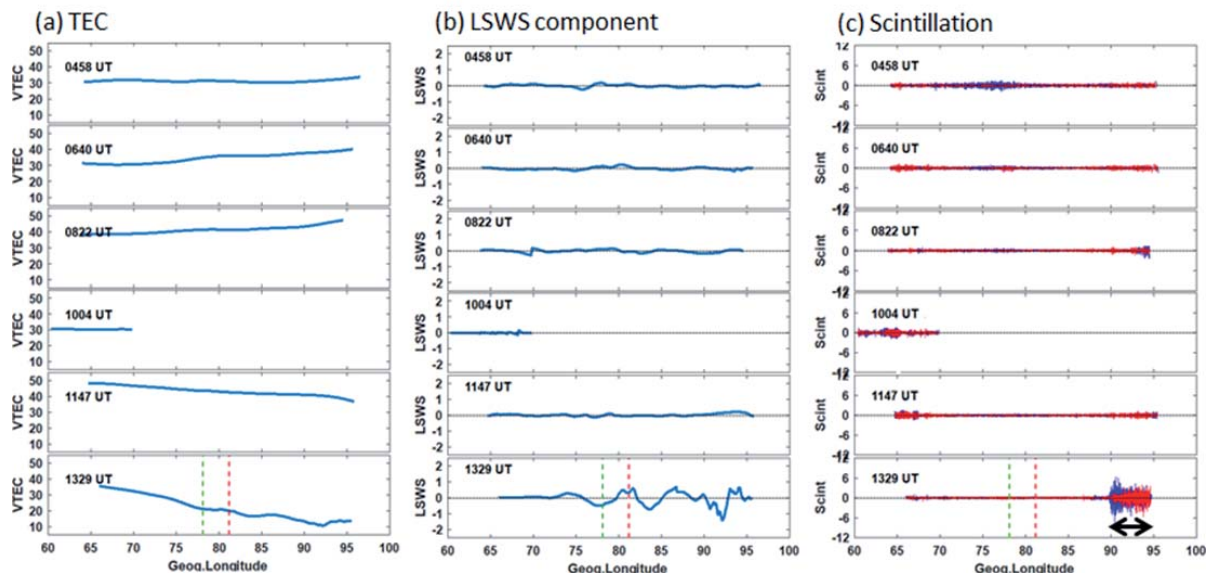
Figure 2. Simultaneous spatial variations of vertical TEC, its large-scale wave-structure component, and amplitude scintillations on 150 MHz and 400 MHz signals observed for six successive orbits of the C/NOFS satellite over Tirunelveli (77.81°E, geomagnetic latitude: 0.08°N). The green and red vertical dotted lines in the bottom panels indicate the locations of the E-region and F-region sunset terminators, respectively. The double-headed arrows in panel (c) indicate amplitude scintillations on both 150 MHz and 400 MHz signals due to the presence of equatorial plasma bubbles on March 31, 2013. The horizontal axis indicates the geographic longitudes of the ionospheric piercing points of the recorded signals (figure courtesy of S. Tulasi Ram).

electric field in the post-sunset equatorial ionosphere, which would raise the equatorial F layer to higher heights, where the ion-neutral collision frequency would be much lower. This would result in a higher growth rate, favoring the occurrence of equatorial spread F. A study of the role of post-sunset equatorial F region vertical plasma drift velocity in the generation and evolution of equatorial spread F using long-term incoherent scatter radar data from the Jicamarca Radio Observatory established that this may be a major cause for the solar-cycle, seasonal, and even day-to-day variability in the occurrence of equatorial spread F [15]. However, longitudinal variability in the occurrence of equatorial spread F, which is characterized by a decorrelation distance as short as a few hundred kilometers, required a more localized explanation. In the early years of study of radar backscatter plumes produced by equatorial spread F irregularities, ALTAIR radar data showed the presence of altitude modulation of electron density contours in the bottom-side of the equatorial F layer prior to plume development [16]. Nearly three decades later, a local upwelling, or quasi-periodic large-scale wave structures (LSWS), on the bottom side of the post-sunset equatorial F layer prior to the occurrence of equatorial spread F started attracting a great deal of attention as a possible source of day-to-day variability in the seeding of the Rayleigh-Taylor instability [17-19]. Figure 2 shows simultaneous observations of spatial variations of vertical total electron content (TEC), its large-scale wave structures component, and amplitude scintillations on 150 MHz and 400 MHz signals observed for six successive orbits of the Communications/Navigation Outage Forecasting System

(C/NOFS) satellite over equatorial station Tirunelveli (77.81°E, geomagnetic latitude: 0.08°N). However, the source for upwelling growth, particularly during periods of low solar activity, has not yet been established.

3. Scintillation Prediction Based on Linear Theory of Rayleigh-Taylor Instability

The early linear and nonlinear theories of equatorial spread F [4] considered only the development of an equatorial plasma bubble in the ionosphere over the dip equator. A two-dimensional cross section of an equatorial plasma bubble involving only coordinates transverse to the geomagnetic field was hence considered. As mentioned in the introduction, the Rayleigh-Taylor instability operating in the equatorial ionosphere gives rise to geomagnetic field-aligned equatorial plasma bubbles, which makes it the largest-scale naturally occurring plasma instability in the Earth's ionosphere. In a two-dimensional theory of the Rayleigh-Taylor instability, variations in ionospheric parameters along the geomagnetic field lines in both the hemispheres was taken into consideration by using geomagnetic flux-tube integrated parameters, following the suggestion of G. Haerendel in his famous unpublished preprint ("Theory of Equatorial Spread F," Max Planck Inst. fur Extraterr. Phys., 1973). Several efforts to predict the occurrence of scintillations have been based on a flux-tube integrated linear growth rate of the Rayleigh-Taylor instability derived by Sultan [20]:

$$\gamma_{RT} = \frac{\Sigma_P^F}{\Sigma_P^F + \Sigma_P^E}\left(V_P - U_L^P - \frac{g_e}{\nu_{eff}^F}\right)K^F - R_T \, . \qquad (1)$$

Here, Σ_P^F and Σ_P^E are flux-tube integrated Pedersen conductivities of the F and E regions of the ionosphere along the geomagnetic field line connecting the equatorial F region with the conjugate E regions in both hemispheres; V_P is the vertical plasma drift at the dip equator due to a zonal electric field; U_L^P is the Pedersen-conductivity-weighted neutral wind perpendicular to the geomagnetic field in the magnetic meridian plane; g_e is the altitude-corrected acceleration due to gravity; ν_{eff}^F is the effective ion-neutral collision frequency weighted by the electron density; K^F is the inverse of the flux-tube electron content vertical gradient scale length; and R_T is the electron density-weighted flux tube recombination rate. In the absence of observational information about the neutral composition, density, and neutral wind, studies of the day-to-day variability in occurrence of equatorial spread F using ionospheric data have focused mostly on the vertical plasma drift at the dip equator, which may be estimated from ionosonde or radar data [15]. In recent years, Carter et al. [21] have used the National Center for Atmospheric Research Thermosphere-Ionosphere-Electrodynamics General Circulation Model (TIEGCM), driven by the solar F10.7 index and the Kp index, to compute the various terms that contribute to the linear growth rate of the Rayleigh-Taylor instability given in Equation (1), to assess the geomagnetic control of equatorial plasma bubble activity and occurrence of VHF and L-band scintillations at five low-latitude stations located at different longitudes. The Kp index characterizes the level of geomagnetic activity. These authors have further used Kp values based on solar-wind data to drive TIEGCM, in an effort to forecast the occurrence of scintillations on GPS signals recorded at some low-latitude stations in the African and Asian longitude sectors [22]. However, there are some major shortcomings in attempts to predict the strength of scintillations at different latitudes based on the linear growth rate of the Rayleigh-Taylor instability. It is only in the nonlinear phase of development of the Rayleigh-Taylor instability that an equatorial plasma bubble rises to the linearly stable topside of the equatorial ionosphere and develops structure [23]. The height to which the equatorial plasma bubbles rise above the dip equator determines the latitudinal extent of scintillations. It is also well known that while strong VHF scintillations are found to occur at dip equatorial locations as well as at locations in the equatorial-ionization-anomaly region where the ambient F peak plasma density may be significantly higher than the dip equatorial F peak plasma density; L-band scintillations show a distinctly different latitudinal distribution. Generally, L-band scintillations tend to be weak at dip equatorial locations, even when strong L-band scintillations are recorded in the equatorial-ionization-anomaly region [24-26]. This has been attributed to the higher background plasma density, N, in the equatorial-ionization-anomaly region F peak, which would result in a higher density fluctuation, ΔN, in the equatorial-ionization-anomaly region compared to the

dip equatorial region, for a given $\Delta N/N$ [26]. However, as discussed in Section 5, enhanced ambient density does not explain the distinctly different relationship between the strengths of VHF and L-band scintillations observed near the dip equator and the equatorial-ionization-anomaly region [27, 28].

4. Scintillation Prediction Based on Three-Dimensional Simulation of Equatorial Plasma Bubble Development?

Equatorial spread F and equatorial plasma bubbles are basically nighttime phenomena. During daytime, currents that flow from the bottom-side of the equatorial F layer, along the geomagnetic field lines for which the electrical conductivity referred to as the direct conductivity is very high, can close through conjugate E layers at the feet of the magnetic field lines, where Pedersen and Hall conductivities are high. This allows currents to flow through
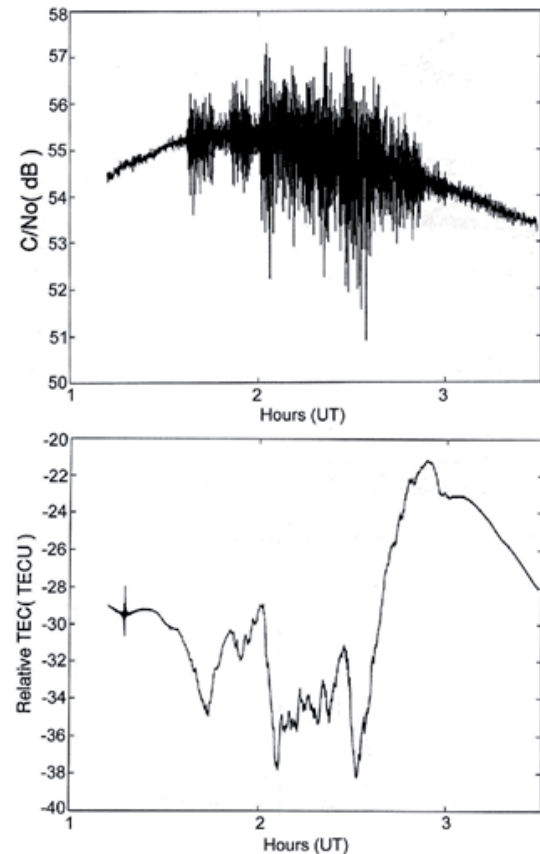

Figure 3. (Top) Fluctuations in the carrier-to-noise ratio on the L1 (1.57542 GHz) GPS signal recorded at an equatorial station, Ancon (77.15°W, geomagnetic latitude 1.07°S), due to amplitude scintillations. (Bottom) The simultaneous variation in relative TEC along the paths of the L1 and L2 (1.2276 GHz) GPS signals recorded at Ancon in the presence of equatorial plasma bubbles (after [34]).

the conjugate E layers in both the hemispheres and back into the bottom-side of the equatorial F-layer, along the nearly perfectly conducting geomagnetic field lines, to short out the perturbation electric field, $\Delta\mathbf{E}$, associated with the Rayleigh-Taylor instability, shown in Figure 1. Once this happens, an equatorial plasma bubble fails to move upwards, and the Rayleigh-Taylor instability does not grow. The time taken to discharge an equatorial plasma bubble is short enough during daytime to prevent the growth of the Rayleigh-Taylor instability [29]. This aspect of equatorial plasma bubble development, as well as mapping of irregularities formed at different altitudes over the dip equator to off-equatorial F regions along geomagnetic field lines, require three-dimensional simulation of the nonlinear development of equatorial plasma bubbles [23, 30-32]. For the computation of scintillation using a phase-screen approximation [10], fluctuations in total electron content (TEC) along the path of an incident radio signal caused by the presence of equatorial plasma bubbles and associated irregularities are used to estimate the phase variations that would be imposed on the incident radio signal by all the irregularities in its path. This information is then used to generate an equivalent phase-changing screen in the path of the signal located near the peak of the F region, and amplitude scintillations are computed [33]. An example of variation in TEC along the paths of the L1 (1.57542 GHz) and L2 (1.2276 GHz) GPS signals recorded at an equatorial station, Ancon, in the presence of equatorial plasma bubbles is shown in the bottom panel of Figure 3. The relative TEC, uncertain to an additive constant, was derived from the respective number of cycles, including fractional cycles, of L1 and L2 carriers recorded by a dual-frequency receiver after it locked onto the signal. Simultaneous variations in the carrier-to-noise ratio on L1 due to amplitude scintillations are shown in the top panel of Figure 3 [34]. Earlier three-dimensional simulations of equatorial plasma-bubble development [30-33] did not have adequate spatial resolution to delineate the intermediate-scale irregularities that cause scintillations on VHF and higher-frequency signals. However, simulation results obtained by Retterer [33], with a spatial resolution of 10 km, showed that in pre-midnight hours, the power spectrum of spatial variations in the magnetic east-west direction of the vertical TEC, down to a scale size of 20 km, was significantly shallower in the equatorial-ionization-anomaly region as compared to the equatorial region. More recently, a high-resolution bubble (HIRB) model was developed by Yokoyama [23], where a zonal resolution of 333.6 m was achieved. With further improvement in spatial resolution and the use of a model with realistically evolving background ionosphere, future high-resolution bubble model simulations would pave the way towards significant progress in prediction of low-latitude ionospheric scintillations. In the absence of realistic three-dimensional simulations of equatorial plasma bubble development with adequate spatial resolution for prediction of scintillations, observations of multi-frequency scintillations at different latitudes may be used to derive important information about the evolution of the irregularities associated with equatorial plasma bubbles that cause scintillations. This aspect is described in the next section, as such information provides a basis for new efforts to predict scintillations at dip equatorial and low latitudes.

5. Latitudinal Distribution of VHF and L-Band Scintillations

As mentioned in Section 3, during pre-midnight hours strong VHF scintillations are often accompanied by moderate-to-strong L-band scintillations in the equatorial-ionization-anomaly region, with the crest of the equatorial-ionization-anomaly region generally located around 15° geomagnetic latitude in the two hemispheres. However, in the dip equatorial region, strong VHF scintillations are accompanied by weak L-band scintillations [24-26]. An example of this is shown in Figure 4. The S_4 index plotted in this figure is the standard deviation of fluctuations in normalized signal intensity, and is used to indicate the strength of amplitude scintillations. In Figures 4a and 4b, respective S_4 indices were computed from amplitude scintillations on a 251 MHz signal transmitted from a geostationary satellite located at 72.4°E and recorded at two locations in the dip equatorial and equatorial-ionization-anomaly regions in the Indian longitude zone. The coordinates of the ionospheric penetration point (IPP) of the signal path at an altitude of 300 km for both of the cases are given in the figures. The geomagnetic latitudes of the ionospheric penetration points were 0.23°S at the dip equatorial location and 9.87°N at the off-equatorial location in the equatorial-ionization-anomaly region. The signal-path elevation angles for the two locations were 78° and 67.6°, respectively. The S_4 indices computed from amplitude scintillations on a 1.575 GHz signal transmitted from the geostationary satellite GSAT-10, located at 83°E, and recorded in dip equatorial and equatorial-ionization-anomaly regions, are shown respectively in Figures 4c and 4d. In this case, the geomagnetic latitudes of the ionospheric penetration points were 0.43°S at the dip equatorial location and 9.81°N at the off-equatorial location in the equatorial-ionization-anomaly region. The signal-path elevation angles for the two locations were 77.8° and 65°, respectively. It is thus seen that for both the VHF and L-band signals recorded at each location, not only are the ionospheric penetration points close enough to assume that the signals were propagating through the same volume of irregularities near the F-region peak, but the elevation angles were also nearly equal. This ensured that the signal-path lengths within the effective irregularity layer near the F-region peak were nearly identical for both the VHF and L-band signals. In the dip equatorial region, strong VHF scintillations were recorded on this day, with the VHF index often exceeding 1. At the same time, L-band scintillations recorded at the equatorial location were weak, with $S_4 < 0.2$. The picture was entirely different in the equatorial-ionization-anomaly region as seen in Figures 4b and 4d. Strong VHF scintillations were recorded here as well, but S_4 did not exceed 1. On the other hand, L-band
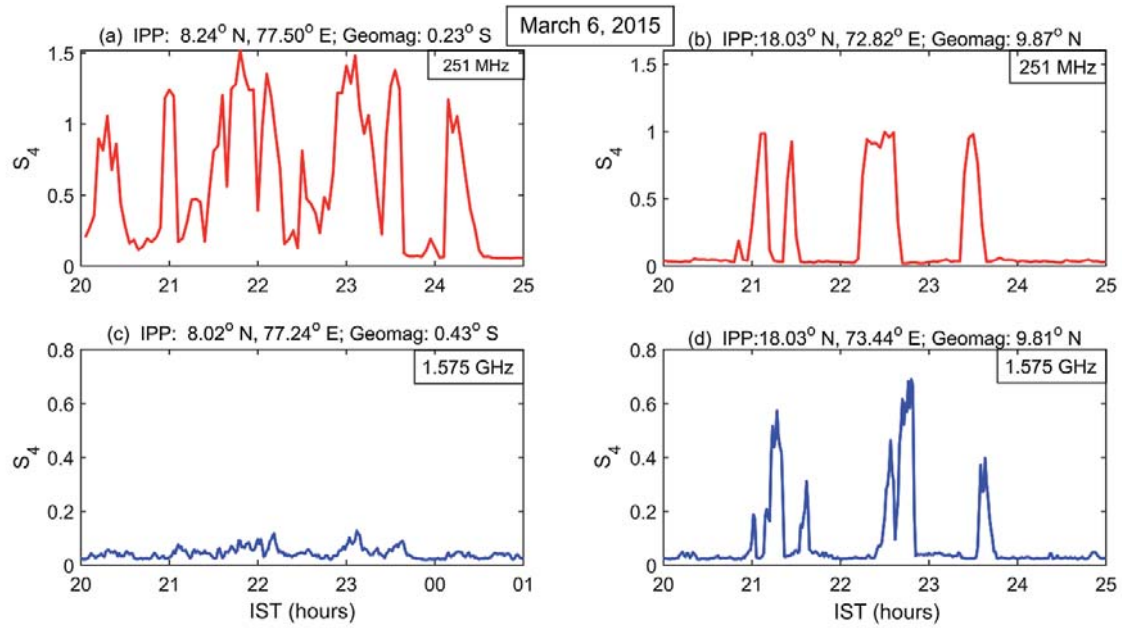
Figure 4. S_4 indices estimated from amplitude scintillations on 251 MHz and 1.575 GHz signals transmitted from geostationary satellites and recorded in dip equatorial and equatorial-ionization-anomaly regions in the Indian longitude zone, as functions of Indian standard time (IST), on March 6, 2015. The coordinates of the respective ionospheric penetration points (IPPs) are given in the figures.

scintillations here were much stronger than near the dip equator. In order to understand how this happened, it was necessary to carry out model calculations of S_4 [27], as described in the next section.

5.1 Model Calculation of S_4 Index

A two-dimensional model of the irregularities is often used to calculate S_4 indices for different irregularity characteristics, since equatorial plasma bubbles and associated irregularities are aligned with the geomagnetic field, assumed to be along the y axis. Since the irregularity-scale sizes involved are much longer than the signal wavelength, radio waves are also essentially scattered in the forward direction close to their propagation paths. The x axis is taken to be in the magnetic east-west direction, so that electron-density variations and associated refractive-index variations depend only on the x and z coordinates. The incident radio wave is assumed to propagate along the z direction. The S_4 index is a special case of the fourth moment, Γ_4, of the complex amplitude, $u(x,z)$, of the radio wave [10]:

$$\Gamma_4\left(x_1, x_2, x_3, x_4, z\right)$$
$$= \left\langle u\left(x_1, z\right) u\left(x_2, z\right) u^*\left(x_3, z\right) u^*\left(x_4, z\right)\right\rangle, \quad (2)$$

where the angular brackets denote an ensemble average. As the signal propagates through the irregularity layer followed by empty space to the ground receiver, Γ_4

satisfies an equation at each point along the path. This equation describes the change in Γ_4 along the propagation path due to contributions from the phase perturbation imposed by the irregularities as well as forward propagation [10]. In situ measurements of plasma-density fluctuations associated with equatorial plasma bubbles in the low-latitude ionosphere using instruments onboard satellites have shown that irregularities in the intermediate-scale range may be described by a power-law type of one-dimensional spectrum [35, 36]. In the two-dimensional models, an isotropic single-component power-law irregularity spectrum with slope $-m$ is often used to characterize the intermediate-scale equatorial spread-F irregularities. A simple power-law spectrum of the form $\Phi_{\Delta N}\left(q\right) \propto q^{-m}$ holds for intermediate scales that are much longer than the inner scale, r_0, and much shorter than the outer scale, R_0, which characterize the irregularity spectra obtained from in situ measurements. The fourth-moment equation may be solved using a split-step method, in which the irregularity layer is considered to consist of multiple phase screens, interspersed with free space between the phase screens [37].

In equatorial plasma bubble simulations, density fluctuations associated with equatorial plasma bubble irregularities are sometimes mentioned as a percentage of the background plasma density, N. However, the strength of scintillations is determined by $\sigma_{\Delta N}$, the standard deviation of electron-density fluctuations, and not by $\sigma_{\Delta N}/N$. In Figure 5, S_4 values for 251 MHz and 1.575 GHz signals – obtained by solving the 4th moment equation [27] – are plotted as functions of $\sigma_{\Delta N}/N$ for a particular background plasma density, N, specified in terms of the
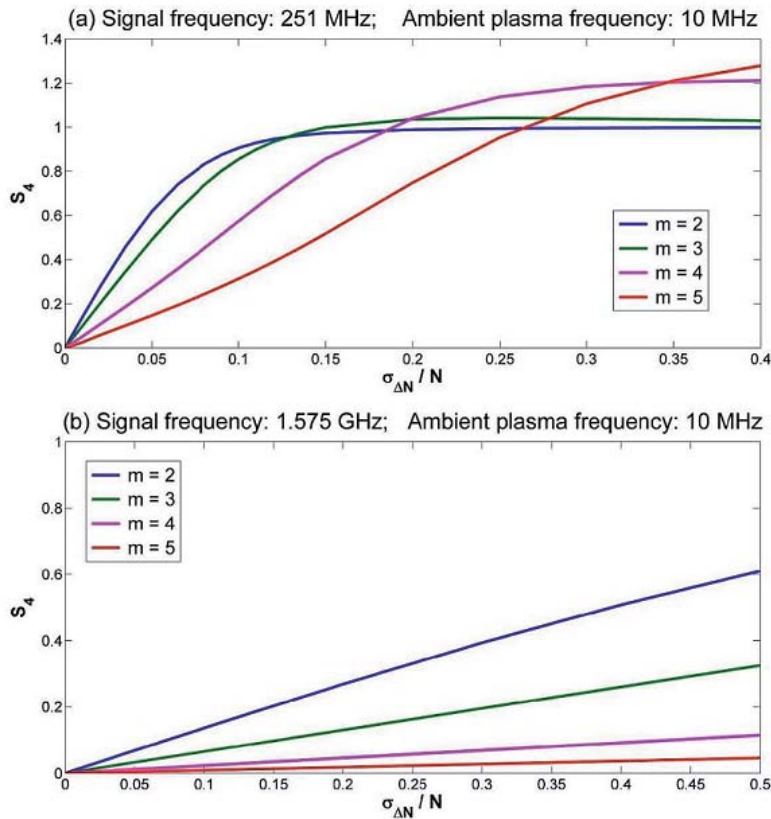
(a) Signal frequency: 251 MHz; Ambient plasma frequency: 10 MHz

Figure 5a. S_4 indices computed for an incident radio signal of frequency 251 MHz as a function of the standard deviation of normalized electron density fluctuations, with N being the ambient plasma density. The irregularities were characterized by a power-law irregularity spectrum with slope $-m$. Four values of m were considered, keeping other irregularity parameters the same (after [27]).

(b) Signal frequency: 1.575 GHz; Ambient plasma frequency: 10 MHz

Figure 5b. The same as for Figure 5a for a signal of frequency 1.575 GHz (after [27]).

ambient plasma frequency, $f_P = \left(Ne^2 / \pi m_e \right)^{1/2}$, where e and m_e are the charge and mass of an electron. An increase in N would imply an increased irregularity strength, $\sigma_{\Delta N}$, for a given $\sigma_{\Delta N}/N$. In this figure, the irregularity power-law spectral index was varied from $m = 2$, which corresponded to a shallow irregularity spectrum, to $m = 5$ corresponding to a steep irregularity spectrum. Other irregularity parameters used to compute S_4 were $r_0 = 10$ m; $R_0 = 10$ km; the thickness of the irregularity layer, $L = 50$ km; and the distance of the ground receiver from the top of the irregularity layer, along the signal path, was 350 km. An important result that emerged from these calculations was that when the irregularities were characterized by a steep power-law spectrum, the L-band S_4 index remained small, even if the irregularity strength was increased by a factor of 10 [27]! However, the VHF S_4 may, in this case, exceed 1 with increasing $\sigma_{\Delta N}$. The VHF result was in agreement with the asymptotic expressions for S_4 derived by Rino [38] for very strong scattering by a one-dimensional phase screen. Those showed that whereas the S_4 index asymptotically approached unity from below for $1 < m < 3$, S_4 may exceed 1 for $m \geq 3$. For steeper spectra, S_4 values greater than 1 were attributed to strong focusing of the signal by larger-scale irregularities, since small-scale structures that are more effective in scattering the radio waves, and therefore destroy the focusing effects of the large-scale irregularities, were absent. These model calculations provided an explanation for the VHF and L-band scintillations observed in the equatorial and equatorial-ionization-anomaly regions [27], an example

of which is seen in Figure 4. At a particular latitude, the maximum contribution to scintillations came from irregularities in the F peak region, where the background plasma density was maximum. This first study of VHF and L-band scintillations in the dip equatorial and equatorial-ionization-anomaly regions showed that the intermediate-scale irregularity spectrum may be much steeper around the equatorial F peak region as compared to the F peak in the equatorial-ionization-anomaly region [27]. High-resolution bubble-model simulations of equatorial plasma bubble development [23] have clearly demonstrated that the topside of the equatorial F region is more structured than the region near the equatorial F peak. In a recent paper [39], high-resolution bubble-model simulation results were used to obtain stochastic structure in evolving equatorial plasma bubbles in three slice planes perpendicular to the geomagnetic field: one at the dip equator and two others at different off-equatorial geomagnetic latitudes. The results showed that structures from the topside of the equatorial F region, above 500 km, were mapped along geomagnetic field lines to the F-region peak (around 350 km) in the offset 2 slice plane. The results obtained from VHF and L-band scintillation observations and modeling may thus be interpreted to indicate that irregularities from the topside of the equatorial F region, which have a shallower spectrum compared to the irregularities near the equatorial F-region peak, map down to F peak in the equatorial-ionization-anomaly region, and cause moderate to strong L-band scintillations when L-band scintillations in the dip equatorial region are weak.

5.2 Signal-Frequency Dependence of Ionospheric Scintillations

As discussed in Section 5.1, a new result that emerged from a study of VHF and L-band scintillations in the dip equatorial and equatorial-ionization-anomaly regions is that the signal frequency dependence of ionospheric scintillations is a pointer to the nature of the power-law spectrum of the equatorial spread-F irregularities that are present in the neighborhood of the F-region peaks at different latitudes, in the post-sunset equatorial and low-latitude ionosphere [27]. Theoretically, the phase-screen approximation has been used to derive the signal-frequency dependence of weak scintillations produced by geomagnetic field-aligned two-dimensional isotropic irregularities characterized by a single-component power-law spectrum with slope $-m$, and with an outer scale much greater than the Fresnel scale ($= \sqrt{2\lambda z_R}$), where z_R is the distance of the phase screen from the receiver. In this case, a simple relationship was found between S_4 and the signal frequency, f : $S_4 \propto f^{-n}$, where $n = (m+3)/4$ [28]. For scintillations that cannot be classified as weak, S_4 indices for 251 MHz and 1.575 GHz signals were computed for varying irregularity strengths by solving the fourth-moment equation as described in Section 5.1. Slopes of the irregularity spectra, assumed to be of power-law form, were varied from -2 to -5. In situ measurements [36] as well as high-resolution bubble-model simulation results indicated that the developed structures within equatorial plasma bubbles were sometimes characterized by a two-component power-law spectrum. No analytical results exist for two-component irregularity spectra. Model computations of S_4 were therefore also carried out for two-component power-law irregularity spectra with a shallow spectral index, $m_1 = 2$, and a steep spectral index, $m_2 = 4$, and break scales varying between 250 m and 4 km. The theoretical results were compared with the frequency exponent, n, derived from amplitude scintillations recorded on a 251 MHz signal and a 1.575 GHz signal transmitted from geostationary satellites and recorded in the dip equatorial and equatorial-ionization-anomaly regions, an example of which is shown in Figure 4. S_4 indices on these two frequencies, f_1 and f_2, were used to obtain n :

$$n(f_1/f_2) = -\frac{\log\left[S_4(f_1)/S_4(f_2)\right]}{\log(f_1/f_2)}. \qquad (3)$$

Comparison of n, as a function of L-band S_4 derived from VHF and L-band scintillations recorded at the two locations on several days, with the theoretical results obtained from model calculations for power-law irregularity spectra with different specifications, clearly showed, for the first time, the distinct nature of the power-law spectra at the two locations. The slope of the irregularity power-law spectrum near the peak of the post-sunset equatorial ionospheric F region was seen to be steep ($m \geq 4$), whereas the irregularity power-law spectrum in the equatorial-ionization-anomaly F peak region was much shallower ($m \leq 2$) before the irregularities started to decay [28]. These results established the critical role of the irregularity spectrum in giving rise to the much stronger L-band scintillations in the equatorial-ionization-anomaly region in comparison to the dip equatorial region. A much higher ambient plasma density would fail to give rise to strong L-band scintillations observed in the equatorial-ionization-anomaly region, if the irregularity power-law spectrum had a slope as steep as that found in the equatorial case. It is thus now clear that for prediction of ionospheric scintillations in the low latitudes, it is necessary to include information of how intermediate-scale irregularities develop at different altitudes within an equatorial plasma bubble under different ambient conditions.

6. Spatial Coherence Scale of Ground Scintillation Pattern

In earlier work using spaced-receiver amplitude scintillation data on a VHF signal transmitted from a geostationary satellite and recorded at a dip equatorial location, the spatial coherence scale of the ground scintillation pattern was studied to understand the evolution of intermediate scale structure within equatorial plasma bubbles in different seasons [40]. Spaced-receiver amplitude scintillation data provides additional information regarding the dynamics of ionospheric irregularities besides the S_4 index and spectrum of scintillations. As seen from Figure 6, other parameters that may be derived from such data include the average drift speed, V_0, of the ground scintillation pattern along the receivers' baseline, and a parameter V_C referred to as a "random" or "characteristic velocity" in the literature [11]. For Figure 6, amplitude scintillation data for a 251 MHz signal recorded by two receivers spaced along a magnetic east-west baseline at an equatorial station were used. As mentioned earlier, movement of the ground scintillation pattern along the receivers' baseline depends on the speed with which irregularities drift across the signal path. The parameter V_C may be related to the standard deviation of fluctuations in irregularity drift [41]. In Figure 6, S_4, V_0, and V_C, computed for each three-minute interval during the scintillation event, were plotted. The parameter $C_I(x_0, t_m)$, where x_0 is the distance between the two receivers, is the maximum cross correlation, found at time lag t_m, for each three-minute interval. This parameter may be used to delineate nascent equatorial plasma bubbles from fossilized equatorial plasma bubbles, for which the perturbation electric field, $\Delta\mathbf{E}$, associated with the Rayleigh-Taylor instability, has decayed, so that the equatorial plasma bubble is not evolving any more. The fossilized equatorial plasma bubbles simply drift with the background plasma as fluctuations in irregularity drift arising from $\Delta\mathbf{E}$ are nearly zero, and the signals recorded by the spaced receivers are well correlated, resulting in $C_I(x_0, t_m)$ values close to unity, as seen in Figure 6
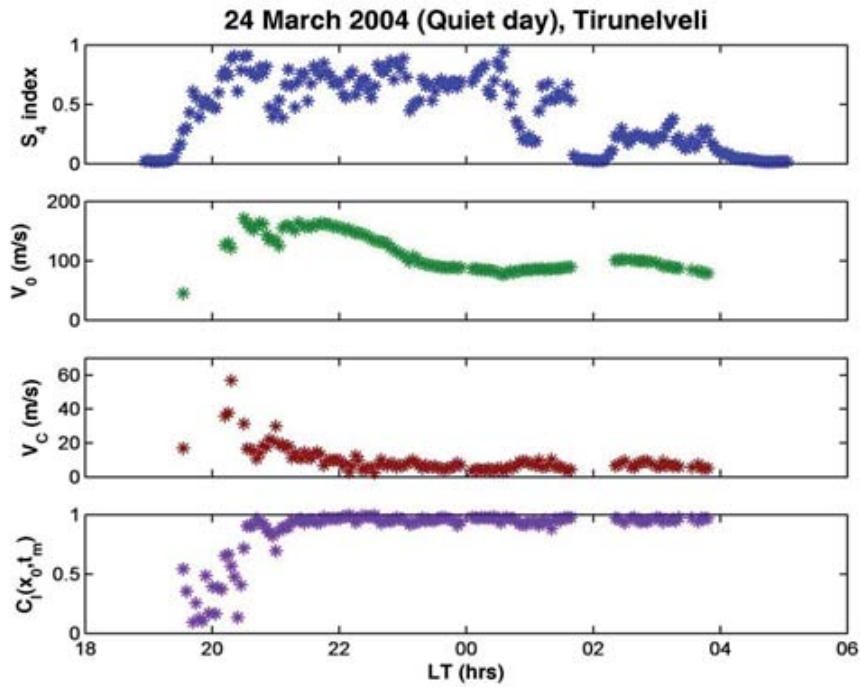
Figure 6. The temporal variation of parameters estimated from amplitude scintillations on a 251 MHz signal transmitted from a geostationary satellite and recorded by two spaced receivers placed 540 m apart along a magnetic east-west baseline at an equatorial station, Tirunelveli. From the top, the parameters were the S_4 index; the average drift speed, V_0, of the ground scintillation pattern along the receivers' baseline; a parameter, V_C, related to the standard deviation of fluctuations in irregularity drift; and the maximum cross correlation between the two signals, $C_I(x_0, t_m)$, where x_0 is the distance between the two receivers and t_m is the time lag for maximum cross correlation. All the parameters were estimated for each three-minute interval during the scintillation event recorded on this day, which was a magnetically quiet day.

[41]. This feature of $C_I(x_0, t_m)$ provides a technique for identifying scintillations produced by equatorial plasma bubbles generated at the longitude of the receiver due to a magnetic storm, as opposed to scintillations caused by irregularities that developed at an earlier time, to the west of the receiver location, and that later drifted eastward with the ambient plasma into the path of the received signal [42]. For the calculation of V_0 and V_C, the space-time correlation function of intensity variations in the ground scintillation pattern was assumed to be of a form that takes into account the possibility of decorrelation of spaced receiver signals [43]:

$$C_I(x,t) = F\left[(x - V_0 t)^2 + V_C^2 t^2\right].$$ (4)

The functional form of F is not required for the computation of V_0 and V_C, but it is assumed that F is a monotonically decreasing function of its argument, with $F(0) = 1$. With the x axis along the baseline of the receivers, which is in the magnetic east-west direction, it is seen from Equation (4) that

$$C_I(x_0, t_m) = F\left[x_0^2 V_C^2 / \left(V_C^2 + V_0^2\right)\right].$$ (5)

In Equation (5), since $C_I(x_0, t_m)$, x_0, V_0, and V_C are estimated from spaced-receiver scintillation data, it is possible to characterize the functional form of F by plotting $C_I(x_0, t_m)$ versus $x_0 V_C / \left(V_0^2 + V_C^2\right)^{1/2}$, as was done in Figure 7. This is equivalent to a plot of the spatial correlation function, $C_I(x, 0)$, as a function of x. It was seen that the spatial correlation functions estimated in this manner were reasonably well approximated by a Gaussian. The ground scintillation pattern for each three-min interval could thus be characterized by a coherence scale length [25]:

$$C_I(x,0) = F\left[x^2\right] = \exp\left[-0.693(x/d_I)^2\right].$$ (6)

Theoretically, the dependence of d_I on the irregularity spectrum may be evaluated by solving the fourth-moment Equation (3) to obtain the spatial correlation function $C_I(x, 0)$ by considering a two-dimensional model of the irregularities, as described in Section 5.1 [40, 44]. For weak scintillations, d_I is basically determined by the Fresnel scale, so that $d_I \propto \sqrt{z_R}$, where z_R is the average distance of the irregularity layer from the receiver along the signal path. There is also a dependence on the spectral index, m, of a power-law spectrum for the irregularities. However, it is not possible to delineate this dependence on

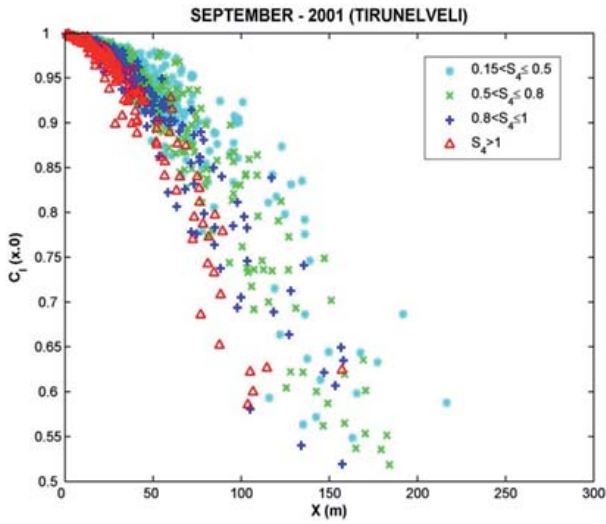**SEPTEMBER - 2001 (TIRUNELVELI)**

Figure 7. A scatter plot of $C_I(x_0, t_m)$ as a function of $x_0 V_C / (V_0^2 + V_C^2)^{1/2}$, which is equivalent to a scatter plot of the spatial correlation function, $C_I(x, 0)$, of the ground scintillation pattern as a function of the spatial lag, x, for each three-minute interval of all the scintillation events recorded by spaced receivers at equatorial station Tirunelveli, on a 251 MHz signal transmitted from a geostationary satellite during the month of September 2001. The points in the plot were color-coded according to the corresponding values of S_4. The four groups of S_4 values extended from weak scintillations ($S_4 \leq 0.5$) to saturated scintillations ($S_4 > 1$). This showed how the coherence scale, which characterizes the ground scintillation pattern, changed with the strength of scintillations.

the spectral slope because as an equatorial plasma bubble evolves, its altitude keeps changing, so that d_I extracted from weak and moderate scintillations would also vary on account of changes in z_R. On the other hand, model

calculations show that for saturated scintillations with $S_4 \geq 1$, d_I becomes independent of z_R, but d_I increases with increasing m: an absence of shorter-scale-length irregularities increases d_I. The dependence of d_I on the spectral slope for saturated scintillations may thus be used to study the evolution of the irregularity spectrum during different stages of equatorial plasma bubble development and decay using spaced-receiver scintillation data [40]. As mentioned earlier, another parameter that is closely linked with equatorial plasma bubble evolution is V_C. In the initial stage of development of an equatorial plasma bubble, V_C rapidly increases. This is the phase when the equatorial plasma bubble rises to the topside of the equatorial F layer, due to the perturbation electric field, $\Delta \mathbf{E}$, associated with the Rayleigh-Taylor instability. Theoretical modeling of the space-time variation of the ground intensity pattern under different scintillation regimes was carried out in the past [11]. It was concluded from these studies that for irregularities that drift across the signal path with an average speed V_0, accompanied by random fluctuations in the drift speed with a standard deviation σ_V, the random velocity, V_C, may be interpreted as a measure of σ_V. The relationship of σ_V with the standard deviation of plasma-density fluctuations produced by the nonlinear growth of the Rayleigh-Taylor instability is as follows [45]:

$$\sigma_V^2 = 0.5 \left(\frac{g}{v_{in}} \right)^2 \left\langle \frac{|\Delta N|^2}{N_0^2} \right\rangle, \qquad (7)$$

where g is the acceleration due to gravity and v_{in} is the ion-neutral collision frequency. After an equatorial plasma bubble stops rising, it comes down to lower altitudes with the downward-drifting ambient plasma to a region of higher v_{in}, resulting in lower σ_V and V_C even while $\sigma_{\Delta N}$ remains the same. The plasma-density structures that give rise to scintillations therefore remain while V_C decreases [41]. The
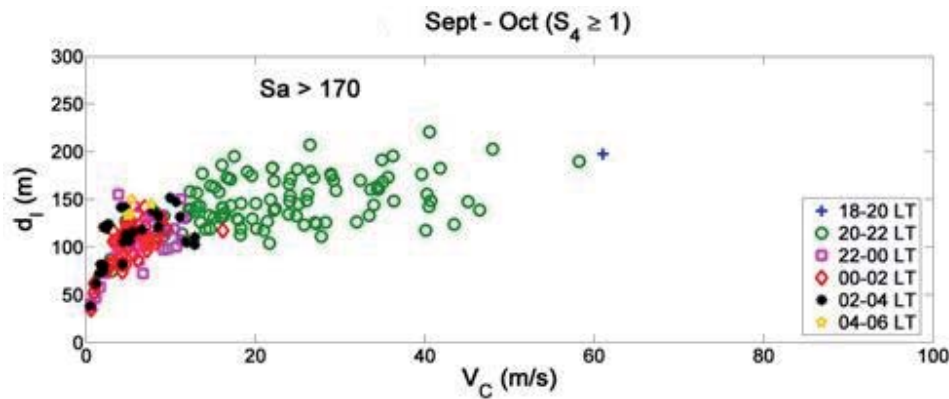

Figure 8. A scatter plot of the coherence scale, d_I, of the ground scintillation pattern as a function of V_C for saturated scintillations ($S_4 \geq 1$) recorded at an equatorial station, Tirunelveli, during scintillation events that occurred in the equinoctial months of September and October on days with high UV solar flux, indicated by the adjusted $F_{10 \cdot 7}$ index (Sa) > 170 during the years 1995-2006. The points were color-coded according to local time (LT). This showed how the ground scintillation pattern changed as the irregularities evolved with time.
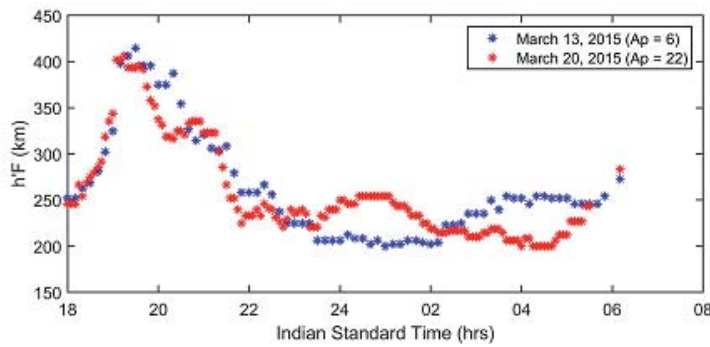
Figure 9. The variation of h′F obtained at the dip equatorial station Tirunelveli during the post-sunset hours of March 13 and 20, 2015 (after [28]).

irregularities finally decay due to diffusion, resulting in the gradual disappearance of scintillations as indicated by the S_4 index. A plot of d_I as a function of V_C for only saturated VHF scintillations ($S_4 \geq 1$) recorded at an equatorial station during a number of scintillation events that occurred in the equinoctial months of September and October on days with high UV solar flux, indicated by adjusted $F_{10·7}$ (Sa) > 170, is displayed in Figure 8. This plot shows that in the initial stages of equatorial plasma bubble development during 20-22 LT (local time), when an equatorial plasma bubble rose rapidly and developed intermediate-scale structure, V_C increased rapidly while d_I, which was independent of height for saturated scintillations, remained nearly constant and had the largest values during a scintillation event recorded in the equatorial region. Comparison with model results for d_I indicated that in the post-sunset equatorial ionosphere, when an equatorial plasma bubble was highly structured on the topside of the equatorial F layer, the irregularity spectrum in the equatorial F peak region was characterized by a steep slope ($m \geq 4$) [40].

7. Latitudinal Extent of Scintillations Due to Equatorial Plasma Bubbles

There are two aspects of the nonlinear development of equatorial plasma bubbles that determine the latitudinal distribution of ionospheric scintillations caused by intermediate-scale irregularities associated with the equatorial plasma bubbles. As discussed in the previous sections, development of structure within the equatorial plasma bubbles as they rise to the topside of the equatorial F layer, and the resulting altitude-dependent irregularity spectra along the magnetic east-west direction over the dip equator, are one set of aspects. This explains the occurrence of weak L-band scintillations near the dip equator when strong L-band scintillations are recorded in the equatorial-ionization-anomaly region. The other aspect of nonlinear development of equatorial plasma bubbles that determines the latitudinal extent of the observed scintillations is the maximum height to which the equatorial plasma bubbles rise. According to a linear theory, in the initial stage of growth of a plasma bubble the magnitude of its velocity of rise over the dip equator is given by [46]

$$V = \frac{\Delta N}{N_0}\left(\frac{g}{\nu_{in}} + \frac{cE_0}{B}\right), \qquad (8)$$

where an ambient equatorial zonal electric field, E_0 which is also generally present has been included, and B is the geomagnetic field at the dip equator. This equation shows that not only the ambient ionospheric conditions but also the thermospheric conditions can significantly alter the initial velocity of rise of an equatorial plasma bubble, because the neutral component comes into the picture through the ion-neutral collision frequency, ν_{in}. However, only a simulation of the nonlinear evolution of equatorial plasma bubbles can provide an answer to the question, When does an equatorial plasma bubble stop rising? Such a simulation demonstrated that an equatorial plasma bubble stops rising when the magnetic-flux-tube-integrated ion-mass density inside the bubble equals that of the surrounding background ionosphere [47]. On magnetically quiet days, post-sunset, the equatorial zonal electric field becomes westward, and the background ionosphere descends even as an equatorial plasma bubble rises through it. There may be two days with a similar rate of descent of the background equatorial ionosphere from the same maximum height, and both days have equatorial plasma bubbles that start developing at the same height. On the day when equatorial plasma bubbles rise at a slower speed, the magnetic-flux-tube-integrated ion-mass density inside a bubble would equal that of the surrounding background ionosphere when the equatorial plasma bubbles are at a lower height. The equatorial plasma bubbles thus would stop rising at a lower height compared to the other day. This impacts the latitudinal extent of scintillations caused by equatorial plasma bubble irregularities. An example of this is presented in Figures 9 and 10. Figure 9 shows the variations of the virtual height, h′F, of the equatorial F layer during the post-sunset hours on a magnetically quiet day, March 13, 2015, and on March 20, 2015, which was preceded by periods of significant magnetic activity. On both days, there was significant pre-reversal enhancement of the eastward electric field in the post-sunset equatorial ionosphere, raising the equatorial F layer to approximately the same maximum height, followed by a descent of the ionosphere at almost the same rate when the ambient electric field turned westward. However, as is evident from Figure 10 where the latitudinal distribution of L-band scintillations is
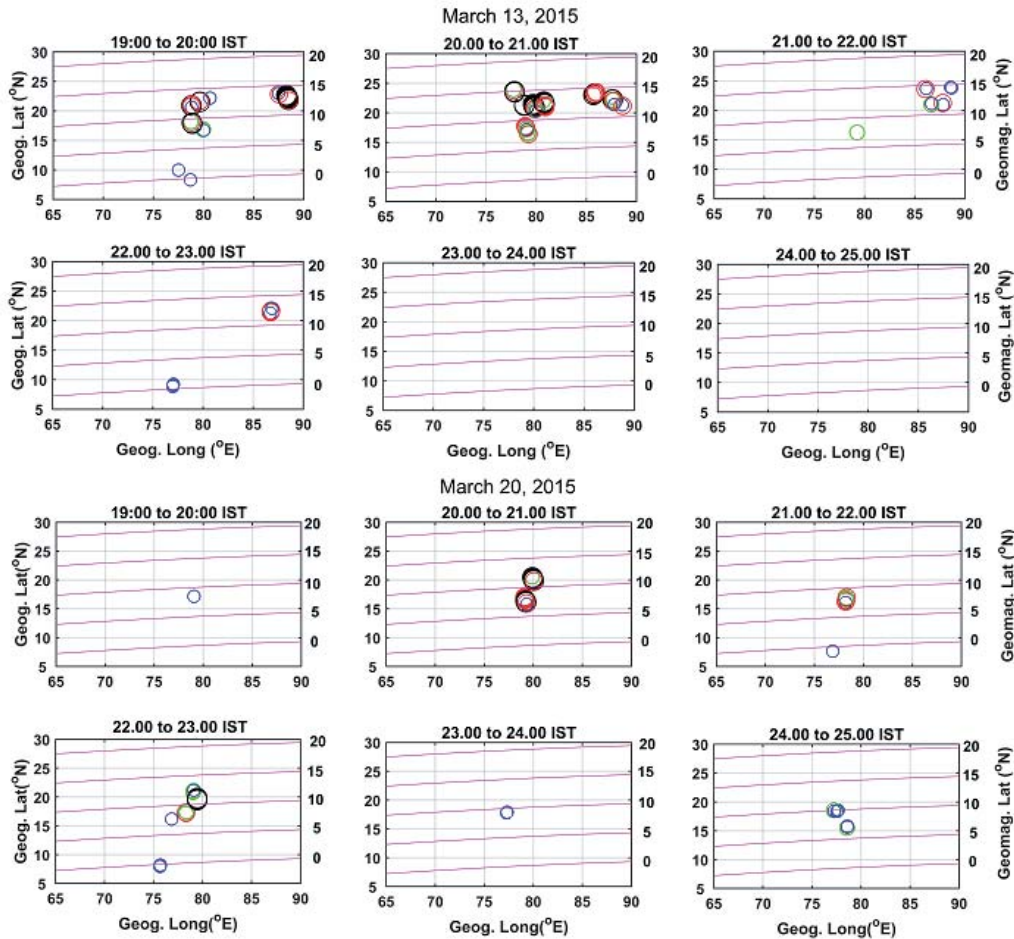
Figure 10. The spatial and temporal variations of L-band scintillations recorded by a network of receivers in the Indian longitude zone for all visible non-geostationary GNSS satellites during periods when the signal-path elevation angle was not less than 55°. The circles of different colors and sizes indicate the levels of five-minute averages of L-band S_4 indices computed along the tracks of the ionospheric penetration points at 300 km altitude for each satellite: (top) on March 13, 2015, and (bottom) on March 20, 2015. Four different levels of S_4 are shown: (1) blue circles for $0.15 \leq S_4 \leq 0.25$; (2) green circles for $0.25 \leq S_4 \leq 0.35$; (3) red circles for $0.35 \leq S_4 \leq 0.5$; and (4) black circles for $S_4 > 0.5$. The geomagnetic latitudes are displayed as mauve lines with the corresponding geomagnetic latitudes at 90°E longitude marked on the right-hand side axes (after [28]).

displayed, the equatorial plasma bubbles stopped rising at a lower height on March 20 as compared to March 13. In the absence of thermospheric data, the Coupled Thermosphere, Ionosphere, Plasmasphere, and Electrodynamics (CTIPe) model was used to determine thermospheric conditions on these two days. The results showed that concentration of atomic oxygen was significantly larger on March 20 compared to March 13, 2015 [48]. Magnetic activity, which is known to alter the post-sunset equatorial zonal electric field on some occasions, and hence to impact the development of equatorial plasma bubbles and associated irregularities that cause scintillations [42], may thus also have a delayed effect on thermospheric density. This alters v_{in}, and hence impacts the maximum altitude to which equatorial plasma bubbles rise, which in turn determines the latitudinal extent of ionospheric scintillations.

8. Conclusions

There have been numerous attempts to predict post-sunset low-latitude ionospheric scintillations [21, 22, 24, 33], as these can give rise to the most deleterious effects on the performance of satellite-based communication and navigation systems such as GNSS, particularly near the crest of the equatorial-ionization-anomaly region, during solar-cycle maximum periods [13, 14]. Nearly all such efforts have been based on the linear growth rate of the Rayleigh-Taylor instability, which is the genesis of the intermediate-scale irregularities that cause scintillations on trans-ionospheric VHF and higher-frequency radio signals. In many studies, some of the ionospheric parameters that appear in the linear growth rate of the Rayleigh-Taylor instability, γ_{RT}, given in Equation (1), have thus been estimated from ionospheric

observations to show their relevance to the prediction of occurrence of scintillations. A lack of information about the thermospheric contributions to γ_{RT} led to the use of coupled thermosphere-ionosphere models, such as TIEGCM (Thermosphere-Ionosphere-Electrodynamics General Circulation Model) for estimation of γ_{RT}, which was considered as the basis for prediction of post-sunset low-latitude scintillations [21, 22]. However, it is clear that prediction of the occurrence of scintillations at off-equatorial latitudes, particularly in the equatorial-ionization-anomaly region, requires knowledge of the nonlinear development of the Rayleigh-Taylor instability, during which phase the equatorial plasma bubbles actually rise to the topside of the equatorial F layer and become structured. These irregularities then map along the geomagnetic field lines to the F-layer peak regions at different off-equatorial latitudes, depending on their height over the dip equator. Understanding this process and its dependence on background parameters calls for three-dimensional simulations of the nonlinear development of the Rayleigh-Taylor instability. Carrying out such simulations using realistic ambient conditions is a big challenge, because the background itself is dynamic [30-32]. Furthermore, until recently the spatial resolution achieved in such simulations was not adequate to study intermediate-scale irregularities involved in giving rise to ionospheric scintillations. For the first time, a sub-kilometer resolution was achieved with the high-resolution-bubble (HIRB) model [23], but the problem of simulating equatorial plasma bubble development in an approximately realistic background ionosphere and thermosphere remains.

As discussed in Sections 5 and 7, the two most important attributes of the irregularities that determine the latitudinal extent and strength of the scintillations are the maximum height attained by the equatorial plasma bubbles as they rise over the dip equator and the spectrum of the intermediate-scale irregularities that develop within the equatorial plasma bubbles at different heights above the dip equator and subsequently map down to off-equatorial latitudes. In the absence of inputs from realistic three-dimensional simulations of the development of equatorial plasma bubbles, in recent years, multi-frequency ionospheric-scintillation data from different locations, spanning the dip equatorial to beyond the equatorial-ionization-anomaly crest latitude in a particular longitude zone, have been used along with model computations of scintillation parameters to deduce the attributes of the irregularities as they develop within equatorial plasma bubbles [27, 28, 40, 48]. These results have provided information that is crucial for the prediction of low-latitude ionospheric scintillations. One of the most important results to emerge is that the long-held belief – that observation of much stronger L-band scintillations in the equatorial-ionization-anomaly region compared to the dip equatorial region is entirely due to the higher background plasma density present in the equatorial-ionization-anomaly region – has been shown to be incorrect. For the first time, crucial dependence of the strength of scintillations, as measured by the S_4 index, on the spectral index of the power-law irregularity spectrum was demonstrated [27, 28]. It was specifically shown that the observed weak amplitude scintillations on L-band signals recorded in the dip equatorial region was due to a steep intermediate-scale power-law irregularity spectrum in the equatorial F peak region. More importantly, it was concluded that if the irregularity spectrum near the peak of the F layer in the equatorial-ionization-anomaly region was as steep as it is in the equatorial F peak region, increasing the background density several fold would not produce the observed strong L-band scintillations near the crest of the equatorial-ionization-anomaly region. As far as the maximum height reached by an equatorial plasma bubble above the dip equator is concerned, the role played by the background thermospheric conditions in this aspect of the nonlinear evolution of equatorial plasma bubbles has been brought out in a recent study of the latitudinal distribution of scintillations due to equatorial plasma bubble irregularities that develop under different background thermospheric conditions when ambient ionospheric conditions are nearly the same [48]. These recent findings undoubtedly make the prediction of low-latitude scintillations more complicated. However, without these critical inputs, attempts to predict scintillations – particularly in the most problematic region near the equatorial-ionization-anomaly crest – based on only the linear growth rate of the Rayleigh-Taylor instability in the dip equatorial region are going to be futile from a practical point of view. The recent results clearly indicate the features that must be explored in the future using high-resolution three-dimensional models of equatorial plasma bubble development under different background conditions, to take the prediction of low-latitude scintillations closer to reality.

9. References

1. L. V. Berkner and H. W. Wells, "F-Region Ionospheric Investigations at Low Latitudes," *Terr. Magn. Atmos. Elec.*, **39**, 3, 1934, pp. 215-230.

2. J. W. Dungey, "Convective Diffusion in the Equatorial F-Region," *J. of Atmos. Terr. Phys.*, **9**, 1956, pp. 304-310.

3. D. T. Farley, B. B. Balsley, R. F. Woodman, and J. P. McClure, "Equatorial Spread F: Implications of VHF Radar Observations," *J. Geophys. Res.*, **75**, 1970, pp. 7199-7216.

4. A. J. Scannapieco and S. L. Ossakow, "Nonlinear Equatorial Spread F," *Geophys. Res. Lett.*, **3**, 1976, pp. 451-454.

5. R. F. Woodman and C. LaHoz, "Radar Observations of F-Region Equatorial Irregularities," *J. Geophys. Res.*, **81**, 1976, pp. 5447-7216.

6. M. C. Kelley et al., "Evidence for a Rayleigh-Taylor Type Instability and Upwelling of Density Depleted Regions During Equatorial Spread F," *Geophys. Res. Lett.*, **3**, 1976, pp. 448-450.

7. C. L. Rino, R. T. Tsunoda, J. Petriceks, R. C. Livingston, M. C. Kelley, and K. D. Baker, "Simultaneous Rocket-Borne Beacon and In Situ Measurements of Equatorial Spread F-Intermediate Wavelength Results," *J. Geophys. Res.*, **86**, 1981, pp. 2411-2420.

8. R. T. Tsunoda, R. C. Livingston, J. P. McClure, and W. B. Hanson, "Equatorial Plasma Bubbles-Vertically Elongated Wedges from the Bottom-Side F Layer," *J. Geophys. Res.*, **87**, 1982, pp. 9171-9180.

9. R. T. Tsunoda, "Magnetic Field-Aligned Characteristics of Plasma Bubbles in the Nighttime Equatorial Ionosphere," *J. of Atmos. Terr. Phys.*, **42**, 1980, pp. 743-752.

10. K. C. Yehand C. H. Liu, "Radio Wave Scintillations in the Ionosphere," *Proc. IEEE*, **70**, 4,1982, pp. 324-360.

11. A. Bhattacharyya, K. C. Yeh, and S. J. Franke, "Deducing Turbulence Parameters from Transionospheric Scintillation Measurements," *Space. Sci. Rev.*, **61**, 1992, pp. 335-386.

12. A. DasGupta, S. Ray, A. Paul, P. Banerjee, and A. Bose, "Errors in Position-Fixing by GPS in an Environment of Strong Equatorial Scintillations in the Indian Zone," *Radio Sci.*, **39**, 2004, RS1S30, doi:10.1029/2002RS002822.

13. J. Aarons, "Global Morphology of Ionospheric Scintillations," *Proc. IEEE*, **70**, 4,1982, pp. 360-378.

14. S. Basu, E. MacKenzie, and Su. Basu, "Ionospheric Constraints on VHF/UHF Communication Links During Solar Maximum and Minimum Periods," *Radio Sci.*, **23**, 1988, pp. 363-378.

15. B. G. Fejer, L. Scherliess, and E. R. de Paula, "Effects of the Vertical Plasma Drift Velocity on the Generation and Evolution of Equatorial Spread F," *J. Geophys. Res.*, **104**, 1999, pp. 19859-19869.

16. R. T. Tsunoda and B. R. White, "On the Generation and Growth of Equatorial Backscatter Plumes 1. Wave Structure in the Bottomside F Layer," *J. Geophys. Res.*, **86**, 1981, pp. 3610-3616.

17. S. V. Thampi, M. Yamamoto, R. T. Tsunoda, Y. Otsuka, T. Tsugawa, J. Uemoto, and M. Ishii, "First Observations of Large-Scale Wave Structure and Equatorial Spread F Using CERTO Radio Beacon on the C/NOFS satellite," *Geophys. Res. Lett.*, **36**, 2009, L18111, doi:10.1029/2009GL039887.

18. S. T. Ram, M. Yamamoto, R. T. Tsunoda, H. D. Chau, T. L. Hoang, B. Damtie, M. Wassaie, C. Y. Yatini, T. Manik, and T. Tsugawa, "Characteristics of Large-Scale Wave Structure Observed from African and Southeast Asian Longitude Sectors," *J. Geophys. Res. Space Physics*, **119**, 2014, pp. 2288-2297.

19. R. T. Tsunoda, S. Saito, and T. T. Ngyuen, "Post-Sunset Rise of Equatorial F Layer – or Upwelling Growth?" *Progress in Earth and Planetary Science,* **5:22,** 2018, doi: 10.1186/s40645-018-0179-4.

20. P. J. Sultan, "Linear Theory and Modelling of the Rayleigh-Taylor Instability Leading to the Occurrence of Equatorial Spread F," *J. Geophys. Res.*, **101**, 1996, pp. 26875-26891.

21. B. A. Carter et al., "Geomagnetic control of Equatorial Plasma Bubble Activity Modeled by the TIEGCM with Kp," *Geophys. Res. Lett.*, **41**, 2014, pp. 5331-5339.

22. B. A. Carter et al., "Using Solar Wind Data to Predict Daily GPS Scintillation Occurrence in the African and Asian Low-Latitude Regions," *Geophys. Res. Lett.*, **41**, 2014, pp. 8176-8184.

23. T. Yokoyama, "A Review on the Numerical Simulation of Equatorial Plasma Bubbles Toward Scintillation Evaluation and Forecasting," *Progress in Earth and Planetary Science,* **4:37,** 2017, doi: 10.1186/s40645-017-0153-6.

24. K. M. Groves et al., "Equatorial Scintillation and Systems Support," *Radio Sci.*, **32**, 1997, pp. 2047-2064.

25. A. Bhattacharyya, K. M. Groves, S. Basu, H. Kuenzler, C. E. Valladares, and R. Sheehan, "L-Band Scintillation Activity and Space-Time Structure of Low-Latitude UHF Scintillations," *Radio Sci.*, **38**, 1, 2003, 1004, doi:10.1029/2002RS002711.

26. J. A. Whalen, "The Linear Dependence of GHz Scintillation on Electron Density Observed in the Equatorial Anomaly," *Ann. Geophys.*, **27**, 2009, pp. 1755-1761.

27. A. Bhattacharyya, B. Kakad, P. Gurram, S. Sripathi, and S. Sunda, "Development of Intermediate-Scale Structure at Different Altitudes Within an Equatorial Plasma Bubble: Implications for L-Band Scintillations," *J. Geophys. Res. Space Physics*, **122**, 2017, pp. 1015-1030.

28. A. Bhattacharyya, P. Gurram, B. Kakad, S. Sripathi, and S. Sunda, "Signal Frequency Dependence of Ionospheric Scintillations: An Indicator of Irregularity Spectrum Characteristics," *J. Geophys. Res. Space Physics*, **124,** 2019, https://doi.org/10.1029/2019JA026987.

29. A. Bhattacharyya, *Role of E Region Conductivity in the Development of Equatorial Ionospheric Plasma Bubbles*," *Geophys. Res. Lett.*, **31**, 2004, L06806, doi:10.1029/2003GL018960.

30. M. J. Keskinen, S. L. Ossakow, and B. G. Fejer, "Three-Dimensional Nonlinear Evolution of Equatorial Ionospheric Spread F Bubbles," *Geophys. Res. Lett.*, **30**, 2003, 1855, doi:10.1029/2005GL017418.

31. J. Huba, and G. Joyce, "Global Modeling of Equatorial Plasma Bubbles," *Geophys. Res. Lett.*, **37**, 2010, L17104, doi:10.1029/2010GL044281.

32. J. M. Retterer, "Forecasting Low-Latitude Radio Scintillation with 3-D Ionospheric Plume Models: 1. Plume Model," *J. Geophys. Res.*, **115**, 2010, A03306,doi:10.1029/2008JA013839.

33. J. M. Retterer, "Forecasting Low-Latitude Radio Scintillation with 3-D Ionospheric Plume Models: 2. Scintillation Calculation,"*J. Geophys. Res.*, **115**, 2010, A03307, doi:10.1029/2008JA013840.

34. A. Bhattacharyya, T. L. Beach, S. Basu, P. M. Kintner, "*Nighttime Equatorial Ionosphere: GPS Scintillations and Differential Carrier Phase Fluctuations*," *Radio Sci.*, **35**, 2000, pp. 209-224.

35. S.-Y. Su, H. C. Yeh, R. A. Heelis, "ROCSAT 1 Ionospheric Plasma and Electrodynamics Instrument Observations of Equatorial Spread F: An Early Transitional Scale Result," *J. Geophys. Res*., **106**, 2001, pp. 29153-29159.

36. F. S. Rodrigues, M. C. Kelley, P. A. Roddy, D. E. Hunton, R. F. Pfaff, O. de La Beaujardiere, and G. S. Bust, "C/NOFS Observations of Intermediate and Transitional Scale-Size Equatorial Spread F Irregularities," *Geophys. Res. Lett.*, **36**, 2009, L00C05, doi:10.1029/2009GL038905.

37. A. Bhattacharyya and K. C. Yeh, "Intensity Correlation Function for Waves of Different Frequencies Propagating Through a Random Medium," *Radio Sci.*, **23**, 1988, pp. 791-808.

38. C. L. Rino, "A Power Law Phase Screen Model for Ionospheric Scintillation, 2. Strong Scatter," *Radio Sci.*, **14**, 1979, pp. 1147-1155.

39. C. Rino, T. Yokoyama, and C. Carrano, "Dynamic Spectral Characteristics of High-Resolution Simulated Equatorial Plasma Bubbles," *Progress in Earth and Planetary Science*, **5:83**, 2018, doi: 10.1186/s40645-018-0243-0.

40. A. Bhattacharyya, B. Kakad, S. Sripathi, K. Jeeva, and K. U. Nair, "Development of Intermediate Scale Structure Near the Peak of the F Region Within an Equatorial Plasma Bubble," *J. Geophys. Res. Space Physics*, **119**, 2014, pp. 3066-3076, doi:10.1002/2013JA019619.

41. A. Bhattacharyya, S. Basu, K. M. Groves, C. E. Valladares, and R. Sheehan, "Dynamics of Equatorial F Region Irregularities from Spaced Receiver Scintillation Observations," *Geophys. Res. Lett.*, **28**,2001, pp. 119-122.

42. A. Bhattacharyya, S. Basu, K. M. Groves, C. E. Valladares, and R. Sheehan, "Effect of Magnetic Activity on the Dynamics of Equatorial F Region Irregularities,"*J. Geophys. Res.*, **107**, 2002, 1489, doi:10.1029/2002JA009644.

43. B. H. Briggs, "The Analysis of Spaced Sensor Records by Correlation Techniques," in R. A. Vincent (ed.), *Middle Atmosphere Program, Handbook for MAP, Vol. 13*, Paris, ICSU, 1984, pp. 166-186.

44. B. Engavale and A. Bhattacharyya, "Spatial Correlation Function of Intensity Variations in the Ground Scintillation Pattern Produced by Equatorial Spread F Irregularities,"*Indian J. of Radio and Space Phys.*, **34,** 2005, pp. 23-32.

45. A. Bhattacharyya, S. J. Franke, and K. C. Yeh, "Characteristic Velocity of Equatorial F Region Irregularities Determined from Spaced Receiver Scintillation Data," *J. Geophys. Res.*, **94**, 1989, pp. 11959-11969.

46. S. L. Ossakow, and P. K. Chaturvedi, "Morphological Studies of Rising Equatorial Spread F Bubbles," *J. Geophys. Res.*, **83,** 1978, pp. 2085-2090.

47. J. Krall, J. D. Huba, S. L. Ossakow, and G. Joyce, "Why Do Equatorial Ionospheric Bubbles Stop Rising?," *Geophys. Res. Lett.*, **37**, 2010, L09105, doi:10.1029/2010GL043128.

48. A. Bhattacharyya, M. Fedrizzi, T. J. Fuller-Rowell, P. Gurram, B. Kakad, S. Sripathi, and S. Sunda, "Effect of Magnetic Storm Related Thermospheric Changes on the Evolution of Equatorial Plasma Bubbles," *J. Geophys. Res. Space Physics*, **124**. 2019,doi:10.1029/2018JA025995.